An Assessment of Impact of Adaptive Notch Filters for Interference Removal on the Signal Processing Stages of a GNSS Receiver

WENJIAN QIN
Politecnico di Torino, Torino, Italy

MICAELA TROGLIA GAMBA
EMANUELA FALLETTI
LINKS Foundation, Torino, Italy

FABIO DOVIS
Politecnico di Torino, Torino, Italy

With the fast growing diffusion of real-time high-accuracy applications based on the global navigation satellite system (GNSS), the robustness of GNSS receiver performance has become a compelling requirement. Disruptive effects can be induced to signal processing stages of GNSS receivers due to the disturbances from radio frequency interference (RFI), even leading to a complete outage of the positioning and timing service. A typical RFI threat to GNSS signals is represented by portable jammers, which transmit swept-frequency (chirp) signals in order to span the overall GNSS bandwidth. The implementation in the receivers of adaptive notch filters (ANFs) for chirp cancellation has been extensively investigated and proved to be an efficient countermeasure. However, the performance of the ANF is strongly dependent on its configuration setup. Inappropriate parameter settings of the ANF for interference removal may induce severe distortion to the correlation process. In addition, an effective mitigation will still introduce a vestigial signal distortion contributed by the residual unmitigated chirp and the ANF operation itself, being not negligible for high-accuracy solutions. This article addresses the detailed analysis for assessing the effects of interference mitigation by notch filtering. A bias compensation strategy is proposed, wherein for each pseudorandom noise, the biases due to parameter settings of the notch filter are estimated and compensated. The impact of using the ANF operation on chirp signals at the acquisition and tracking stages of GNSS receivers is analyzed. On the basis of the three proposed metrics, the effects can be quantitatively estimated to depict a complete picture of the most influential parameters of the chirp and the ANF configurations, as well as the optimal achievable performance at the acquisition and tracking stages.

Manuscript received November 10, 2019; revised February 28, 2020 and March 23, 2020; released for publication March 28, 2020. Date of publication April 28, 2020; date of current version October 9, 2020.

DOI. No. 10.1109/TAES.2020.2990148

Refereeing of this contribution was handled by D. Qiu.

The work of W. Qin was supported by the European Union's Horizon 2020 Research and Innovation Programme through the TREASURE project under the Marie Skłodowska–Curie Actions grant agreement No. 722023.

Authors' addresses: Wenjian Qin and Fabio Dovis are with the Department of Electronics and Telecommunications, Politecnico di Torino, 10129 Torino, Italy E-mail: (wenjian.qin@polito.it, fabio.dovis@polito.it); Micaela Troglia Gamba and Emanuela Falletti are with the Space and Navigation Technologies Area, LINKS Foundation, 10138 Torino, Italy E-mail: (micaela.trogliagamba@linksfoundation.com; emanuela.falletti@linksfoundation.com). *(Corresponding author: Wenjian Qin.)*

I. INTRODUCTION

Extensive applications of positioning and navigation solutions based on the global navigation satellite system (GNSS) increasingly demand robustness of GNSS receiver performance. Disruptive effects can be induced to the signal processing stages of GNSS receivers due to the presence of radio frequency interference, leading to degraded estimation of position, velocity, and time (PVT) or eventually a complete denial of the receiver service [1]. Such interference threats rapidly expand with the increasing number of wireless communication infrastructures that can potentially transmit signals at frequencies close to the allocated GNSS bands as unintentional disturbances [2] as well as the effect of natural interferences, which are not negligible when dealing with high-accuracy performance [3]. In addition, a more severe threat is posed by personal privacy devices, widely known as jammers, which are used to intentionally broadcast powerful signals with carrier frequency varying over GNSS bands in a target area, in order to cause an outage of the GNSS-based service [4], [5]. The widely explored precorrelation techniques aim to detect and mitigate interference with advanced digital signal processing techniques before the correlation process performed in the GNSS receiver. Because of various interference types, the mitigation methods are expected to customize for specific interference characteristics.

Considering the extremely low power of the received GNSS signals, an efficient interference mitigation solution demands a good tradeoff between the preservation of useful GNSS signals and the effective cancellation of the interference. Different types of interference affect GNSS signals in different ways, causing distortion of the ranging code and affecting the correlation process.

Many precorrelation approaches have been proposed so far in the literature based on the techniques in the time domain [6], [7], the frequency domain [8], the time–frequency domain [9], and the transformed domain [10], [11]. The adaptive filter techniques can be implemented for interference suppression [12], among which the infinite impulse response (IIR)-based adaptive notch filter (ANF) is particularly appealing due to its low complexity and low computational load [13], [14]. The ANF is the evolution of the notch filter (NF), which is characterized by a passband frequency response that remains constant for the largest part of the frequency domain, but it rejects a narrow portion of the spectrum in correspondence of the interference. The NF has

been proved to be effective on the mitigation of continuous wave interference (CWI) [13], narrow-band interference [15], [16], and pulsed interference [17]; thus, it has been preferably implemented into the high-end GNSS receivers for interference removal. A more challenging scenario is the countermeasure for swept-frequency (chirp) jamming signals. With an additional adaptive block, the ANF is capable of tracking the frequency variation of the chirp signals [14]. Equivalent modifications on the adaptive block by employing frequency-locked loop (FLL) theory are further proposed [18] and extensively discussed [19], [20]. According to [21], the regular ANF and FLL-equivalent ANF architectures show comparable performance.

In addition, the procedure of mitigation operation itself may also bring nonnegligible distortion to the GNSS signals. The effects of the NF operation on the acquisition and tracking stages have been addressed in the literature by exploiting specific metrics for evaluation. In [13], the code distortion introduced by the NF operation at the acquisition stage in the absence of interference is evaluated quantitatively by calculating the loss of the signal-to-noise ratio (SNR) at the correlation output. Analysis shows that the degradation of the SNR due to the NF operation is related to the shift frequency and rejection bandwidth of the notch with respect to the code spectrum. Such an SNR loss varies with different code structures but shows negligible difference for different pseudorandom noise (PRN). A further exploration on the effects at the tracking stage is conducted in [22]–[24]. In [22], the bias and jitter caused by the NF operation with different shift frequencies and rejection bandwidths in the absence of interference are qualitatively estimated with a proposed metric called asymmetry coefficient. In [24], the effects of different NF methods on autocorrelation function distortion are estimated.

However, the analysis of the effects of the NF in the signal processing stages of GNSS receivers is still far from being fully covered, and this article addresses additional topics to enrich and complete the investigation. The analysis in [13], [22], and [23] is implemented under the assumption that no interference exists, whereas the presence of interference makes the distortion analysis more complex. In fact, code distortion is the result of a combined effect of both the NF and the residual unmitigated interference. Another tricky problem is the analysis of ANF effects for chirp signal removal. The parameters of the adaptive block that control the convergence capability of the ANF should be carefully tuned. Inappropriate parameter settings of the ANF would lead to unsuccessful chirp mitigation, as it will be shown in this article.

The distortion analysis at the acquisition and tracking stages due to the ANF operation for the chirp signal removal has been preliminarily investigated in [21] and [25]. The metrics of α_{mean}, interference error envelope (IEE), and code jitter are selected to quantitatively assess the distortion and thus to evaluate the ANF efficiency. This article extends such preliminary results to a comprehensive analysis of the effects.

The rest of this article is organized as follows. Section II introduces signal and system models. A description of mitigation techniques is given in Section III. Section IV outlines the assessment tools for distortion analysis. Comparative analysis of two simulation scenarios is addressed in Sections V and VI, respectively. The former provides an estimation of the distortion caused by the NF operation for CWI removal at the tracking stage, and the latter extends the discussion to the effects of the ANF for chirp cancellation in the complete signal processing chain of GNSS receivers. Finally, Section VII concludes this article.

II. SIGNAL AND SYSTEM MODELS

A general scheme of a GNSS receiver is depicted in Fig. 1, where the GNSS signals are received at the antenna, further downconverted to the intermediate frequency (IF), filtered, and digitalized at the front-end. An additional precorrelation mitigation unit is employed to implement advanced detection and mitigation techniques. In the signal processing chain of a GNSS receiver, the acquisition stage is designed to perform a rough estimation of the code delay and the Doppler frequency of the incoming GNSS signals, and the tracking stage is exploited to finalize the estimation progressively through tracking loops. PVT values are eventually obtained on the basis of the output at the tracking stage.

In a scenario where the interference is present, the received signals after the analog-to-digital converter at the front-end can be modeled as

$$r[n] = \sum_{k=1}^{N} s_k[n] + \eta[n] + i[n] \tag{1}$$

where $r[n]$ is the received signal at IF, $s_k[n]$ is the GNSS signal collected from the kth satellite, $\eta[n]$ is the additive Gaussian noise, $i[n]$ is the interference, and n is the discrete time index. $s_k[n]$ can be defined as

$$\begin{aligned} s_k[n] = {} & A_k c_k(nT_s - \tau_k) h_k(nT_s - \tau_k) d_k(nT_s - \tau_k) \\ & \times \exp\left\{ j2\pi \left(f_{\text{IF}} + f_d^k \right) nT_s + j\phi_k \right\} \end{aligned} \tag{2}$$

where A_k is the signal amplitude, c_k is the spreading code, h_k is the subcarrier, d_k is the navigation data, T_s is the time sampling interval, τ_k is the code delay, f_{IF} is the IF, f_d^k is the Doppler frequency, and ϕ_k is the carrier phase.

The interference component $i[n]$ can be modeled differently according to the interference type. A detailed classification and description of the interference types is addressed in [1]. In this article, two specific types of interference, i.e., CWI and linear chirp, are considered for the test scenarios. The value of the carrier-to-interference ratio (C/I), i.e., the ratio between the power strength of the GNSS signal with respect to the interference power, will be used to characterize the different scenarios.

A complex CWI, represented as a spectral line in the frequency domain, can be defined as

$$i_{\text{cw}}[n] = A_{\text{cw}} \exp\{ j2\pi f_i n T_s + j\phi_i \} \tag{3}$$

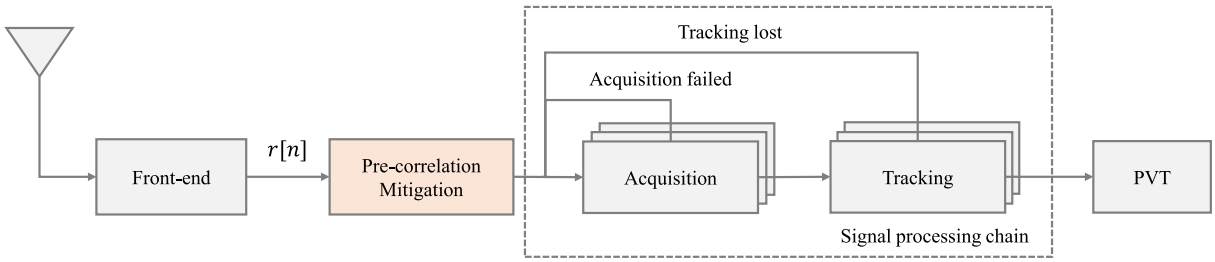

Fig. 1. General scheme of a GNSS receiver.

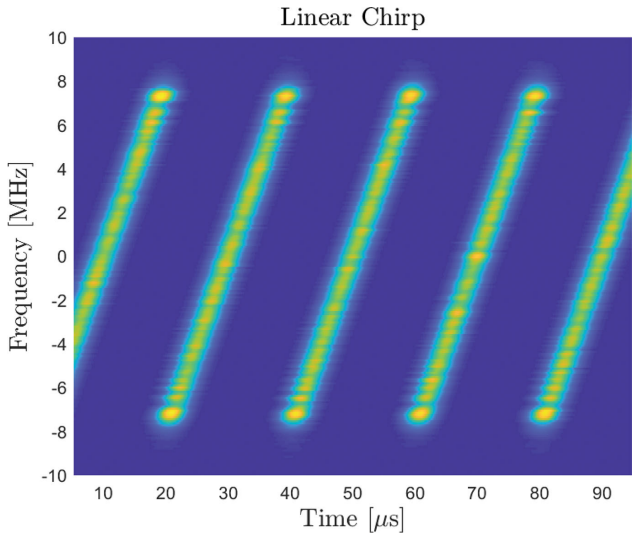

Fig. 2. Spectrogram of a GPS L1 signal interfered by a linear chirp, with $B_n = 16\,\text{MHz}$, $T_p = 20\,\mu\text{s}$, $v_s = 0.8\,\text{MHz}/\mu\text{s}$, $f_c = 0\,\text{MHz}$, and $C/I = -50\,\text{dB}$.

where A_{cw} is the CWI amplitude, f_i is the CWI frequency, and ϕ_i is the CWI phase.

A linear chirp is characterized by the linear variation of the carrier frequency over a frequency bandwidth named sweep range B_n within one chirp period T_p.

The linear chirp signal in one period T_p can be modeled as

$$i_{\text{cp}}[n] = A_{\text{cp}} \exp\left\{ j2\pi f_0 n T_s + j2\pi v_s (nT_s)^2/2 + j\phi_{\text{cp}} \right\} \quad (4)$$

where A_{cp} is the chirp amplitude, f_0 is the starting frequency of the sweep range, v_s is the sweep rate, defined as $v_s = B_n/T_p$, and ϕ_{cp} is the chirp phase. The central frequency of the chirp can be obtained as $f_c = f_0 + B_n/2$.

The spectrogram of a GPS L1 signal interfered by a linear chirp is shown in Fig. 2 as an example. The values for B_n and T_p are the ones of a typical chirp signal broadcasted by a mass-market jammer, as reported in [5].

III. MITIGATION TECHNIQUES

The theoretical model of the IIR-based ANF has been proposed and extensively discussed in the literature [13], [14]. In general, the architecture of the ANF can be regarded as a combination of the NF and an additional adaptive block, which are briefly reviewed in the following.

A. Notch Filter

The one-pole NF can be employed to suppress complex CWI. As already addressed in [13], the transfer function of a one-pole NF is given by

$$H(z) = \frac{1 - z_0 z^{-1}}{1 - k_\alpha z_0 z^{-1}} \quad (5)$$

where $k_\alpha \in [0, 1)$ is the pole contraction factor regulating the width of the notch and z_0 is the zero of the transfer function to be placed at the frequency in correspondence of the interference. The relation between z_0 and the notch frequency f_{nf} can be expressed as

$$z_0 = \exp\left(j2\pi f_{\text{nf}} T_s\right) \quad (6)$$

where z_0 is forced to move on the unit circle. An ideal notch for the cancellation of CWI expressed in (3) is obtained when $f_{\text{nf}} = f_i$ with a very small rejection bandwidth, thus preserving the most useful GNSS signals. According to [1], the 3-dB attenuated bandwidth of the NF can be approximately calculated as

$$B_{3\text{dB}} \approx (1 - k_\alpha) f_s \pi / 10 \quad (7)$$

which indicates that a larger k_α close to 1 leads to a smaller notch bandwidth, with f_s being the sampling frequency.

The one-pole NF can be further extended to two-pole and multipole NFs to suppress the real CWI with two or multiple spectral lines in the frequency domain [14].

B. Adaptive Block

In order to track the frequency span of the swept-frequency signals, adaptive techniques are proposed in [14] and [18], leading to two ANF architectures, denoted as the regular ANF and the FLL-equivalent ANF, respectively. The former estimates the frequency of the interfering signal through the stochastic-gradient-based technique, and the latter employs FLL-based techniques.

In the regular ANF [14], z_0 is enabled to move in the complex plane and converge to the interference through a least-mean-square-based iterative rule to progressively calculate z_0 at run-time

$$z_0[n] = z_0[n-1] - \mu[n]\, g(J[n]) \quad (8)$$

where $\mu[n]$ is the algorithm step, $J[n]$ is the cost function to be minimized, and $g(.)$ is the stochastic gradient of the cost function.

To properly obtain the adaptive algorithms, the transfer function (5) can be written as a cascade of autoregressive (AR) and moving average (MA) blocks, and there are different ways to set the blocks [13], [18]. According to [18], the MA output is given by

$$y_m[n] = r[n] - z_0 r[n-1] \tag{9}$$

where $r[n]$ is the received interfered signal defined in (1).

The output of the filter $x_f[n]$ corresponding to (5) can be expressed as

$$x_f[n] = r[n] - z_0 r[n-1] + k_\alpha z_0 x_f[n-1] \tag{10}$$

and $x_r[n]$ is the output of the AR block, given by

$$x_r[n] = r[n] + k_\alpha z_0 x_r[n-1]. \tag{11}$$

As proposed in [14] and [18], the cost function in (8) can be designed either to minimize the expectation of the NF output energy as $J[n] = E\{|x_f[n]|^2\}$ or to minimize the expectation of the MA output energy as $J[n] = E\{|y_m[n]|^2\}$. $\mu[n]$ in (8) is the algorithm step [26], given by

$$\mu[n] = \frac{\delta}{E\{|x_r[n]|^2\}} \tag{12}$$

where $E\{|x_r[n]|^2\}$ is the expectation of AR output energy and δ controls convergence.

The activation of the ANF is determined by comparing the modulus of the averaged z_0 to a predefined threshold T_h. The value of T_h is selected based on the interference-to-noise ratio (I/N) considered harmful to the receiver. The averaged z_0 is given by

$$\hat{z}_0[n] = \alpha \hat{z}_0[n-1] + (1-\alpha) z_0[n] \tag{13}$$

where α is the forgetting factor.

The performance of the ANF is strongly dependent on the parameter settings. k_α (notch width) and δ (convergence capability) are the two most influential parameters to shape the ANF and are expected to be carefully tuned. A smaller rejection bandwidth (k_α close to 1) will preserve the most useful GNSS signals but will also bring the difficulty to the adaptive block to track the frequency variation. Inappropriate values of the parameters may lead to strong distortion to the useful signals, even more severe than the distortion caused by the interference; thus, a good tradeoff is always demanded.

IV. ASSESSMENT TOOLS FOR DISTORTION ANALYSIS

The distortion induced by the interference and the ANF operation on the ranging code can affect the result of the correlation process between the received signals and the local code replica. The assessment tools selected for the distortion analysis provide approaches to quantitatively estimate the impairment of the interference and the ANF operation at both the acquisition and tracking stages, by employing three metrics: peak-to-noise-floor ratio, code bias, and code jitter. The methodology employed to assess these metrics is briefly described in the following sections.

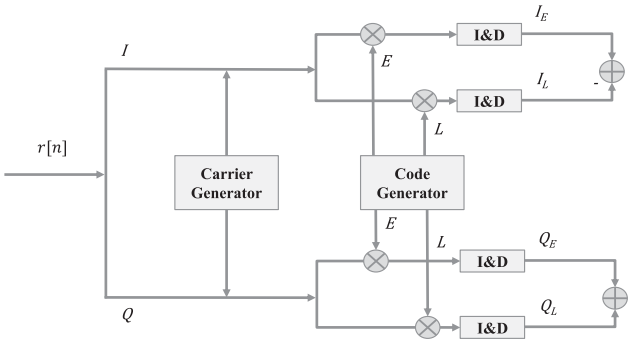

Fig. 3. Open-loop code discriminator.

A. Assessment of the Peak-to-Noise-Floor Ratio

In acquisition, the correlation peak of the cross-ambiguity function (CAF) is searched and α_{mean} is defined as a way to measure the correlation peak-to-noise-floor ratio in [1], and it is given by

$$\alpha_{\text{mean}} = 20 \log_{10}\left(\frac{x_p}{E_i}\right) \tag{14}$$

where x_p is the correlation peak of the CAF and E_i is the average of i off-peak correlation points in the search space.

The increasing power of the interference will lead to the loss of α_{mean}, thus causing an increasing probability of a false alarm during the acquisition process [1]. When the ANF is implemented, the value of α_{mean} can also indicate the ANF efficiency with different parameter settings. The use of α_{mean} for ANF parameter optimization is proposed in [21], with the benefit of employing a metric easy to assess directly at the acquisition stage of a GNSS receiver.

B. Assessment of the Code Bias

In code tracking, the delay-locked loop (DLL) discriminator (S-Curve) is exploited to measure the residual error between the estimated code delay and the true code delay of the incoming signal. The presence of interference and the ANF operation will affect not only the correlation process, but also the output of the DLL discriminator.

The concept of IEE has been proposed and discussed in [27] and [28], and it is based on an open-loop code discriminator in the absence of noise to quantitatively measure the code biases with respect to one or more characteristics of the interfering signal (e.g., interference frequency and phase). The IEE is depicted as a plot of the maximum and minimum values of the ranging errors versus the chosen interference parameters.

In an open-loop code discriminator, as illustrated in Fig. 3, it is assumed that the Doppler frequency and the code delay are perfectly estimated in the in-phase and quadrature branches. The correlation is then performed between the incoming signal and the local early and late replicas, and correlation distortion is due to the interference and the ANF operation.

The receiver configuration can be adjusted in terms of discriminator function, correlator spacing, and integration

time. A coherent early–late discriminator function $R_{EL,C}$ is employed in [28], expressed as

$$R_{EL,C} = I_E - I_L \tag{15}$$

where I_E and I_L are the output of the early and late in-phase correlators.

Similarly, a noncoherent discriminator function can be used for the evaluation. Many options of noncoherent discriminator functions have been proposed [29], and there is a freedom to choose one for the investigation. The same discriminator function $R_{EL,NC}$ has been considered for the bias and jitter analysis, given by

$$R_{EL,NC} = \frac{1}{2}\frac{\left(I_E^2 + Q_E^2\right) - \left(I_L^2 + Q_L^2\right)}{\left(I_E^2 + Q_E^2\right) + \left(I_L^2 + Q_L^2\right)} \tag{16}$$

where Q_E and Q_L are the output of the early and late quadrature correlators.

As already demonstrated in [28], coherent and noncoherent discriminators lead to negligible difference on the IEE estimation, and the same also applies for different correlator spacing ($\Delta \leq 1$ chip). This finds explanation in the assumption of perfect phase-locked loop and DLL, thus implying that the GNSS signal power is fully recovered in the in-phase branch only. This is true for the unfiltered signal, while in the case of a one-pole NF, some GNSS signal power also will be split to the quadrature branch after the filtering operation, thus showing different results if a noncoherent discriminator is applied.

Without loss of generality, in this article, the IEE analysis has been entirely conducted considering only the coherent discriminator function in (15), and the applied methodology can be extended to different discrimination rules. Two code structures, i.e., binary phase-shift keying (BPSK) and binary offset carrier BOC (1, 1), are simulated for the assessment of IEE, with the integration time of 1 and 4 ms, respectively.

C. Assessment of the Code Jitter

The IEE mainly reflects the bias induced at the zero-crossing point of the S-Curve, but such bias is not the only relevant effect. In this regard, as investigated in [28], in the presence of CWI, the S-Curve around the zero-crossing point shows to be still linear and parallel to the ideal one, i.e., the interference-free S-Curve. As the power of CWI increases, the S-Curve looks more deformed but is still in a regular shape, while in the presence of a chirp signal and after the filtering operation, the S-Curve proves to be strongly distorted with an irregular shape, as discussed later in Section VI. In other words, zero bias alone is not sufficient to guarantee a successful DLL convergence to the zero-crossing point if the S-Curve is severely distorted. Thus, the overall shape deformation of the S-Curve also should be considered as an extra assessment of linearity loss, in addition to the bias induced at the zero-crossing point.

In this regard, the code jitter is employed as the metric to quantitatively evaluate such overall shape deformation. It is obtained as the normalized standard deviation of the tracking error in the steady-state condition in the presence of additive noise [30]. While the IEE tool provides an approach to evaluate the most influential characteristics of both the interference and the ANF configurations, the value of the code jitter can indicate the noisiness of the ranging errors and the filtering efficiency.

In this case, a closed-loop DLL architecture is considered: the null-seeker structure is implemented to continuously seek the null at the output of the discriminator, in order to provide a fine estimation of code delay in the presence of additive noise. The discriminator function $R_{EL,NC}$ expressed in (16) is used in simulation scenarios, with spacing $\Delta = 1$ chip and the integration time of 1 ms.

V. BIAS ANALYSIS: CWI VERSUS NF

The analysis first addresses the case of CWI and NF, based on the metric of IEE. This is an extension to the study on the IEE for CWI discussed in [27] and [28]. All the simulations are performed considering a digital version of the GNSS signals. The GNSS signal is generated by the N-FUELS Signal Simulation Tool [31]. A MATLAB-based Software-Defined Radio GNSS receiver is used in order to implement the mitigation methods and analyze the performance [32].

A. S-Curve

In Fig. 4, the S-Curve is depicted as an example to demonstrate the possible distortion induced by CWI and NF operation. The zero-crossing point of the S-Curve for $\tau \in [-\frac{\Delta}{2}, \frac{\Delta}{2}]$ chip refers to the lock point of the DLL at the tracking stage, and the existence of a bias will lead to a ranging error in the estimated pseudorange. Line 1 in Fig. 4 shows the ideal S-Curve of a clean input GPS L1 signal, with the zero-crossing point located exactly at the zero delay. A noticeable bias is induced to the zero-crossing point when the signal is interfered by a CWI with carrier frequency centered at 0.5 MHz away from the GPS L1 carrier with $C/I = 0$ dB, as shown by line 2, whereas the overall shape of the S-Curve around the lock point still keeps parallel to the interference-free case represented by line 1.

Lines 3 and 4 illustrate the S-Curve distorted by narrow NFs with $k_\alpha = 0.99$ and $k_\alpha = 0.95$, respectively, in the absence of interference. It can be observed that not only biases are introduced, but also the slopes of the S-Curve around the lock point are different and no longer parallel to line 1. Furthermore, with $k_\alpha = 0.95$, the induced bias is even larger than the interfered case of line 2. This result clearly points out how it is important to activate the NF only when the presence of the interfering signal is detected.

Finally, the CWI described above is mitigated by means of an ideal NF with the same k_α indicated before and placed at the exact frequency of the CWI. Thus, lines 5 and 6 show the distorted S-Curve due to both the NF operation and the residual unmitigated CWI, with $k_\alpha = 0.99$ and $k_\alpha = 0.95$, respectively. Compared to lines 3 and 4, the biases at the

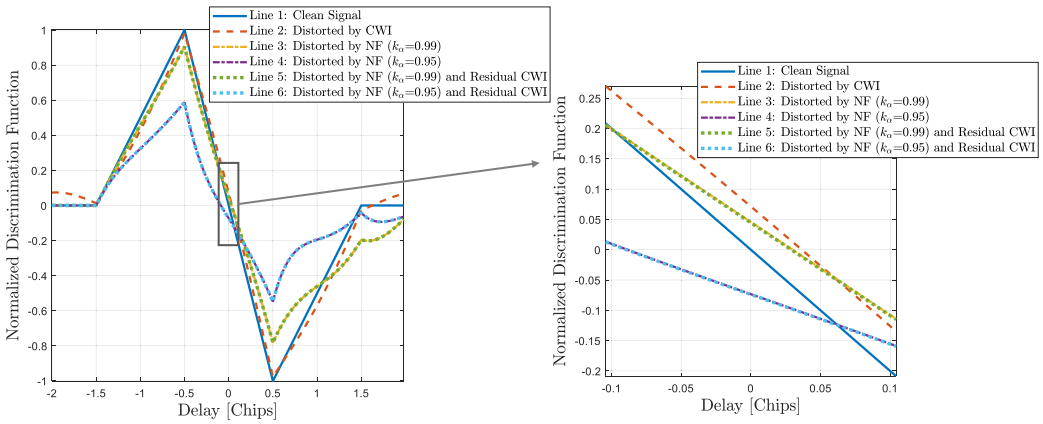

Fig. 4. Example of the induced distortion on S-Curve by CWI and NF for BPSK (GPS L1, PRN 1).

zero-crossing point after the CWI mitigation exhibit negligible differences, thus proving that the CWI is efficiently mitigated and the remained biases are mainly due to the NF operation, while the contribution of the residual unmitigated CWI is nearly irrelevant. This means that in the presence of a weak CWI, as is the case, the NF operation may degrade performance more than the interference itself in the GNSS receivers, thus making the mitigation not so convenient. As a general observation, a good mitigation of the CWI by means of NF does not guarantee to nullify the bias; on the contrary, a residual bias resulting from the combination of the filtering operation and the unfiltered interfering power can be observed.

Both CWI and NF operation can cause distortion of the S-Curve, as better explained hereafter by the analysis of the theoretical model.

According to [28], the coherent discriminator function (15) under interference can be written as

$$R_{\mathrm{EL}}^{\mathrm{si}}[n] = R_{E}^{\mathrm{si}}[n] - R_{L}^{\mathrm{si}}[n] \tag{17}$$

where the superscripts s and i stand for the GNSS signal component and the interference component, respectively, with $R_{E}^{\mathrm{si}}[n] = I_E$ and $R_{L}^{\mathrm{si}}[n] = I_L$. In this regard, $R_{\mathrm{EL}}^{\mathrm{si}}[n]$ can be rewritten by splitting into two terms, as follows:

$$R_{\mathrm{EL}}^{\mathrm{si}}[n] = R_{\mathrm{EL}}^{s}[n] + R_{\mathrm{EL}}^{i}[n] \tag{18}$$

where the distorted discriminator function $R_{\mathrm{EL}}^{\mathrm{si}}[n]$ can be regarded as the sum of two components $R_{\mathrm{EL}}^{s}[n]$ and $R_{\mathrm{EL}}^{i}[n]$, which are, respectively, the ideal S-Curve and the induced distortion due to the interference. Under the assumption that the Doppler frequency and the code delay are perfectly estimated, the two terms can be modeled by simply employing the convolution theory

$$R_{\mathrm{EL}}^{s}[n] = \frac{1}{NL}\left(c_E[n] - c_L[n]\right) * s_c[-n] \tag{19}$$

$$R_{\mathrm{EL}}^{i}[n] = \frac{1}{NL}\left(c_E[n] - c_L[n]\right) * i[-n] \tag{20}$$

where N refers to the number of integration periods, L is the samples per code period, and $*$ is convolution. $c_E[n]$ and $c_L[n]$ are the local early and late code replicas, respectively. $s_c[n]$ is the code component of the input GNSS signal and $i[n]$ is the CWI.

The total bias at the zero-crossing point of the distorted discriminator function $R_{\mathrm{EL}}^{\mathrm{si}}[n]$ in (18) is then the sum of two components:

$$b_{\mathrm{EL}}^{\mathrm{si}} = b_{\mathrm{EL}}^{s} + b_{\mathrm{EL}}^{i} \tag{21}$$

where b_{EL}^{s} is a deterministic component with zero bias obtained from the ideal S-Curve $R_{\mathrm{EL}}^{s}[n]$ and b_{EL}^{i} is the induced bias due to the distortion term $R_{\mathrm{EL}}^{i}[n]$.

Similarly, the coherent discriminator function after the implementation of the NF can be written as the sum of two terms, as follows:

$$R_{\mathrm{EL}}^{\mathrm{si,nf}}[n] = R_{\mathrm{EL}}^{s,\mathrm{nf}}[n] + R_{\mathrm{EL}}^{i,\mathrm{nf}}[n] \tag{22}$$

where the superscript nf stands for the NF operation. Based on (19) and (20), $R_{\mathrm{EL}}^{s,\mathrm{nf}}[n]$ and $R_{\mathrm{EL}}^{i,\mathrm{nf}}[n]$ can be further modeled as

$$R_{\mathrm{EL}}^{s,\mathrm{nf}}[n] = \frac{1}{NL}\left(c_E[n] - c_L[n]\right) * s_c[-n] * h_{\mathrm{nf}}[n] \tag{23}$$

$$R_{\mathrm{EL}}^{i,\mathrm{nf}}[n] = \frac{1}{NL}\left(c_E[n] - c_L[n]\right) * i[-n] * h_{\mathrm{nf}}[n] \tag{24}$$

where $h_{\mathrm{nf}}[n]$ is the discrete impulse response of the NF.

Finally, the total bias of the distorted discriminator function $R_{\mathrm{EL}}^{\mathrm{si,nf}}[n]$ in (22) after the implementation of the NF at the zero-crossing point can be written as

$$b_{\mathrm{EL}}^{\mathrm{si,nf}} = b_{\mathrm{EL}}^{s,\mathrm{nf}} + b_{\mathrm{EL}}^{i,\mathrm{nf}} \tag{25}$$

where $b_{\mathrm{EL}}^{s,\mathrm{nf}}$ is a deterministic component with bias obtained from the S-Curve $R_{\mathrm{EL}}^{s,\mathrm{nf}}[n]$, and $b_{\mathrm{EL}}^{i,\mathrm{nf}}$ is the induced bias due to the term $R_{\mathrm{EL}}^{i,\mathrm{nf}}[n]$.

As shown in Fig. 4, there are four types of S-Curve considered in different scenarios, and each of them can be represented as one of the discriminator functions expressed above. The reference S-Curve (line 1) refers to the discriminator function $R_{\mathrm{EL}}^{s}[n]$ in (19), with zero bias $b_{\mathrm{EL}}^{s} = 0$. The S-Curve distorted by CWI (line 2) refers to the discriminator function $R_{\mathrm{EL}}^{\mathrm{si}}[n]$ in (18), with $b_{\mathrm{EL}}^{\mathrm{si}} = b_{\mathrm{EL}}^{i}$. $R_{\mathrm{EL}}^{s,\mathrm{nf}}[n]$ in (23) and $R_{\mathrm{EL}}^{\mathrm{si,nf}}[n]$ in (22) are the discriminator functions distorted by the NF operation, respectively, in the absence of interference

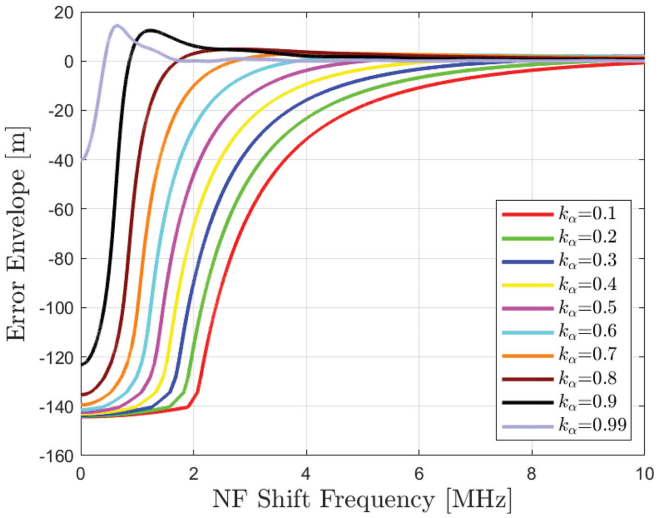

Fig. 5. NEE for BPSK (GPS L1, PRN 1), with $\Delta = 1$ chip.

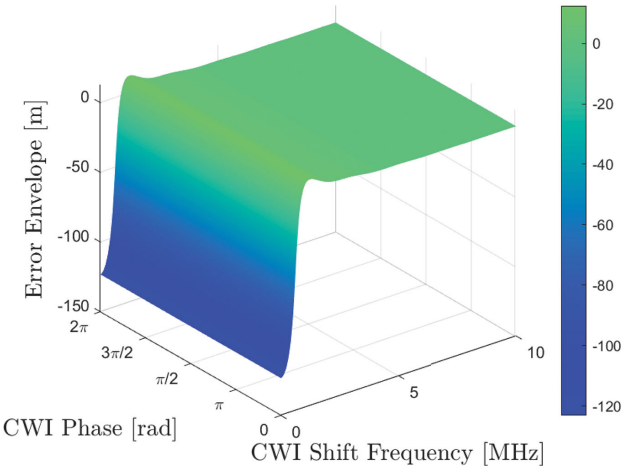

Fig. 6. Error envelope versus CWI phase and CWI shift frequency after NF mitigation for BPSK (GPS L1, PRN 1), with $k_\alpha = 0.9$.

(lines 3 and 4) and in the presence of the CWI (lines 5 and 6). The total bias $b_{\mathrm{EL}}^{\mathrm{si,nf}}$ in (25) is then contributed by both the NF operation and the residual interference. Furthermore, if the signals and the parameter settings of the NF are fixed, for each PRN, the deterministic bias $b_{\mathrm{EL}}^{s,\mathrm{nf}}$ in (25) can be estimated and compensated. In fact, this bias is related to z_0, k_α, and the PRN number. As a result of this compensation process, the contribution due to the residual unmitigated CWI after NF operation, i.e., the term $b_{\mathrm{EL}}^{i,\mathrm{nf}}$, can be isolated and evaluated. In addition, rather than code-domain compensation, the same filter could be applied to the replica code to compensate the phase distortion induced by the filter [26]. It is also possible to implement a zero-phase filter offline using a recursive filter twice both forward and backward in time [33].

B. Error Envelope

In order to extend the above analysis, the metric of IEE is further employed and implemented to estimate the induced bias of the S-Curve versus the variable characteristics of both CWI and NF. Similarly, the concept of IEE can be extended to assess the ranging errors due to the NF operation itself, in the absence of interference. The most influential characteristics of the one-pole NF introduced in Section III are the notch frequency and the rejection bandwidth. In this regard, a plot of the ranging errors versus the notch shift frequency, with different values of the pole contraction factor k_α (i.e., different bandwidths of the notch), is depicted in Fig. 5. This type of error envelope affected by the NF operation only, without interference effects, for the sake of clarity will be called as notch error envelope (NEE).

As shown in Fig. 5, the largest bias due to the NF operation comes at $f_{\mathrm{nf}} \sim 0$ MHz for all k_α, and the ranging errors gradually reduce toward to zero with overshoot-like behavior. Furthermore, a narrower notch (k_α close to 1) only affects a small portion of the frequency bandwidths, while a wider notch shows more severe influence on larger bandwidths of the code spectrum.

In the remainder of this estimation, the CWI is mitigated using an ideal NF, i.e., placing the notch at the true frequency of the CWI (i.e., $f_{\mathrm{nf}} = f_i$) in order to ensure the most effective mitigation. For this analysis, several values of the notch rejection bandwidth have been considered. The ranging errors are then contributed by both the NF operation and the residual CWI. In Fig. 6, the error envelope for the filtered CWI as a function of the CWI phase and frequency is shown as an example, with $k_\alpha = 0.9$. In Fig. 7, the obtained maximum and minimum values of the ranging errors over all CWI phases versus the CWI shift frequency for different values of k_α are then depicted. It can be observed that the overall shape of the IEE for the filtered CWI is very similar to the NEE in Fig. 5, thus further confirming that the CWI is efficiently cancelled and the distortion induced by NF is by far dominant with respect to the residual unmitigated CWI.

As previously discussed, it is possible to estimate the deterministic term $b_{\mathrm{EL}}^{s,\mathrm{nf}}$ referring to the bias induced by the NF operation in (25), to achieve the compensated bias $b_{\mathrm{EL}}^{i,\mathrm{nf}}$ due to the residual unmitigated CWI. The compensation operation can be implemented for the IEE in Fig. 7 by subtracting the values of ranging errors in the NEE, as depicted in Fig. 5. Fig. 8 illustrates the compensated error envelope for CWI after NF mitigation as a function of CWI phase and shift frequency, with $k_\alpha = 0.9$. Fig. 9 then presents the extracted maximum and minimum values of the ranging errors. It can be observed that the compensated errors in Fig. 9 are very small, showing a symmetric trend that is similar to the IEE for CWI, as shown in [28].

Different receiver configurations and code structures lead to different resilience to the impairment induced by the NF operation. In Fig. 10, it can be observed that with a smaller spacing of the discriminator, the overall induced ranging error is reduced. Furthermore, a BOC (1, 1) modulated signal shows more resilience to the narrow notch than BPSK when $f_{\mathrm{nf}} \sim 0$ MHz, as demonstrated in Fig. 11.

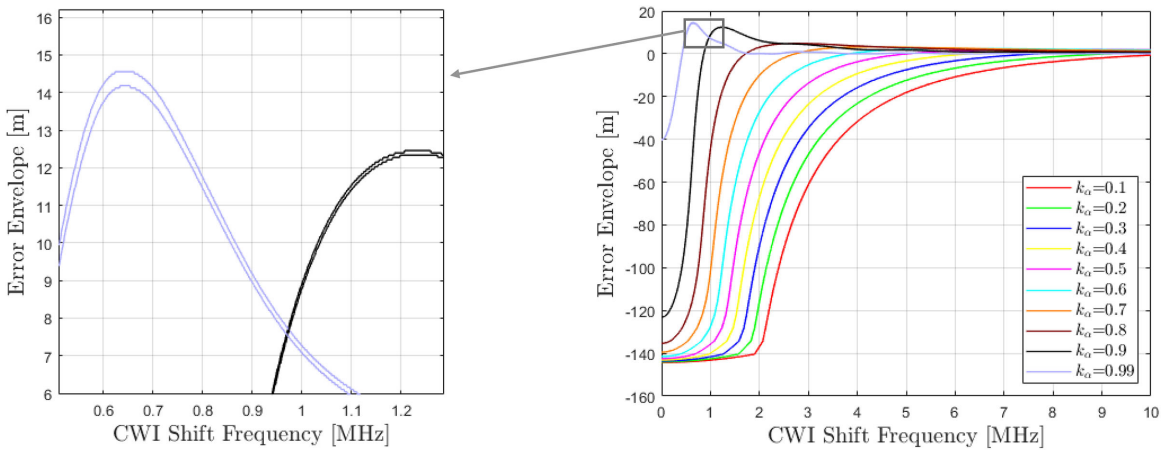

Fig. 7. IEE for CWI after NF mitigation for BPSK (GPS L1, PRN 1).

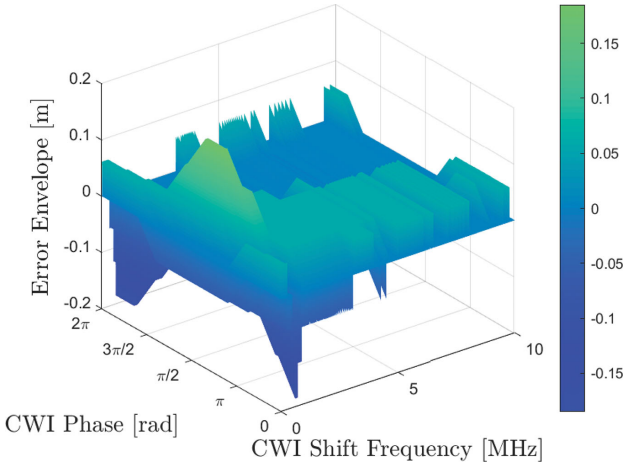

Fig. 8. Error envelope versus CWI phase and CWI shift frequency after NF mitigation and compensation process for BPSK (GPS L1, PRN 1), with $k_\alpha = 0.9$.

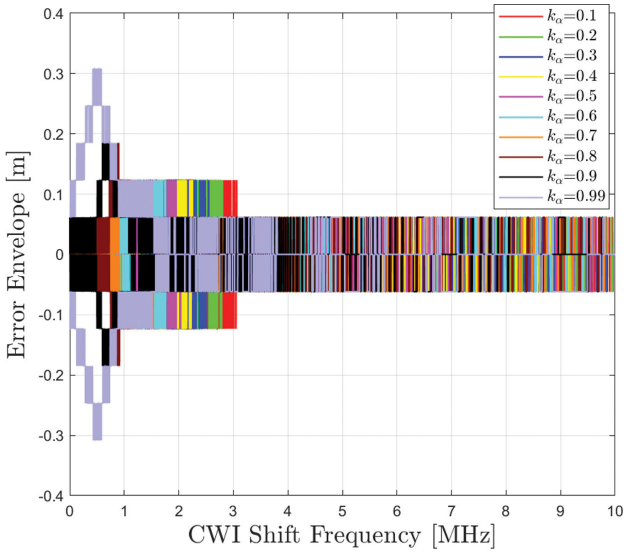

Fig. 9. IEE for CWI after NF mitigation and compensation process for BPSK (GPS L1, PRN 1).

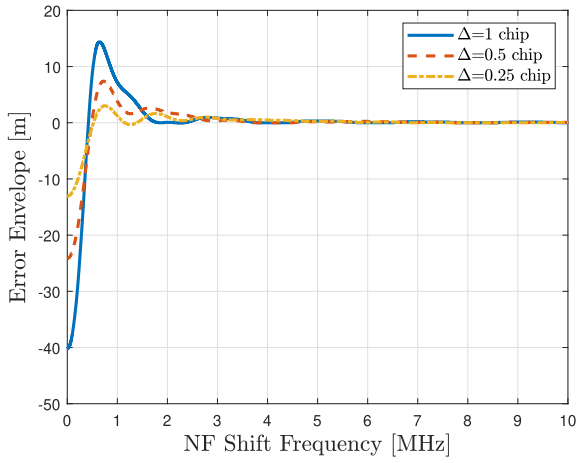

Fig. 10. NEE for BPSK (GPS L1, PRN 1), with $k_\alpha = 0.99$ and different discriminator spacing.

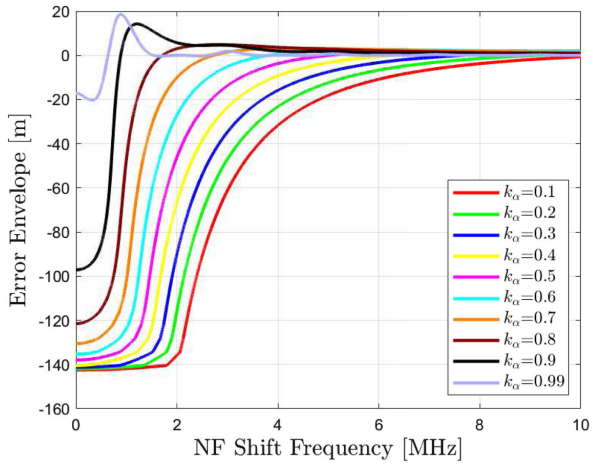

Fig. 11. NEE for BOC (1, 1), with $\Delta = 1$ chip.

VI. COMPARATIVE ANALYSIS ON THE IMPAIRMENT: CHIRP VERSUS ANF

In the previous section, a fixed frequency interference was considered to show the effects due to the NF. In this

TABLE I
Simulation Setup

Simulation Parameters		Units	For Bias Analysis	For α_{mean} and Jitter Analysis
Receiver Configuration	Sampling frequency (f_s)	MHz	49.104	49.104
	Intermediate Frequency (IF)	MHz	0	0
	Spacing (Δ)	chip	0.25, 0.5, 1	1
	Coherent integration time	ms	1, 4	1
	Non-coherent integration time	ms	/	1
GPS L1 Signal	PRN	/	1	1
	Power (P_{L1})	dBW	0	-157
	Carrier-to-Noise ratio (C/N_0)	dB − Hz	noise free	55
Galileo E1b Signal	PRN	/	1	/
	Power (P_{E1})	dBW	0	/
	Carrier-to-Noise ratio (C/N_0)	dB − Hz	noise free	/
Chirp Signal	Power (P_{cp})	dBW	0, 10, 20, 30	-107
	Sweep range (B_n)	MHz	4, 8, 12, 16	16
	Sweep period (T_p)	μs	6, 10, 20, 33	20
	Sweep rate (v_s)	MHz/μs	0.48, 0.8, 1.6, 2.7	0.8
	Central frequency (f_c)	MHz	$[0 \div 10]$ (spaced of 1 kHz)	0
	Chirp phase (ϕ_{cp})	rad	$[0 \div 2\pi]$ (spaced of $\pi/5$)	0
	Carrier-to-Interference ratio (C/I)	dB	-30, -20, -10, 0	-50

section, the assessment of the impairment induced by the chirp signal and the ANF operation is performed on the basis of the three metrics introduced in Section IV.

A. Simulation Scenario

Digital linear chirp signals are simulated at baseband according to the parameters of the real chirp signals investigated in [5] and combined to the GPS L1 and Galileo E1b signals (without data) simulated by the N-FUELS at IF level. It is assumed that the sweep ranges of the simulated chirps are within the pass bandwidth of the front-end. The 16-MHz bandwidth chosen for the jammer sweep range is justified by the fact that the high-end receivers may use wide front-end bandwidth to exploit all the signal components on L1/E1 bands (e.g., time-multiplexed BOC and composite BOC) and to better characterize multipath and interference with appropriate signal processing. Thus, narrow-band filtering effects due to the front-end, which may distort the chirp pattern, are not considered in this article. The definition of the parameters that characterize the chirp signals has been described in Section II, and a full list of the simulation parameters is given in Table I.

B. α_{mean} Analysis

The evaluation process on the effect of the ANF for chirp removal is carried out based on α_{mean} at the acquisition stage of the receiver. As reference, the value of α_{mean} in an interference-free scenario is first calculated as 47.9 dB, whereas α_{mean} for the scenario suffering the chirp signal with parameters described in Table I is 20.3 dB, leading to an unsuccessful acquisition. The loss of α_{mean} between the interference-free case and the interfered case can be regarded as the impairment due to the interference. The ANF is then implemented for the chirp cancellation with different parameter settings. The degradation of α_{mean} after the ANF operation is caused by both the ANF operation and the residual unmitigated interference, and this effect can be quantitatively evaluated by comparing it against to the interference-free case.

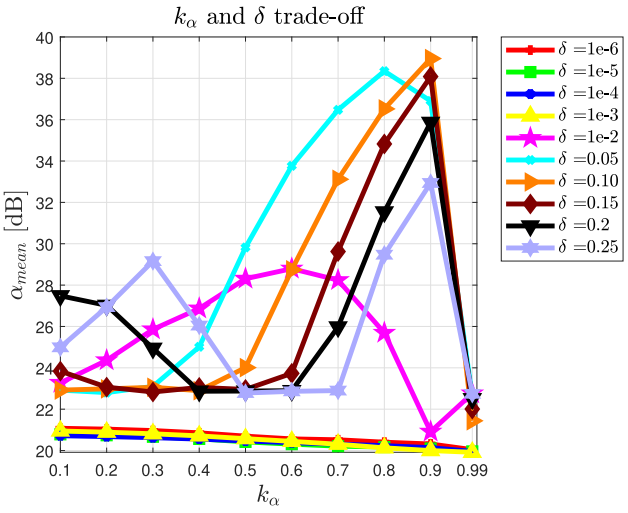

Fig. 12. k_α and δ tradeoff based on α_{mean}, with $B_n = 16$ MHz, $T_p = 20\,\mu$s, and $C/I = -50$ dB.

Additionally, the ANF efficiency is also reflected by comparing the values of α_{mean} with different parameter settings, and in this way, an optimization procedure can be performed. As introduced in Section III, k_α and δ are the two most influential parameters to regulate the performance of the ANF and demand for a good tradeoff. In Fig. 12,

the values of α_{mean} with different k_α and δ are presented. The choice of δ is based on the empirical values, and k_α changes between 0 and 1, representing different rejection bandwidths of the notch. The threshold T_h and the forgetting factor α in (13) are fixed to $T_h = 0.7$ and $\alpha = 0.9$, respectively. A direct picture of the optimal performance achievable by the ANF for chirp removal is illustrated. It can be seen that inappropriate parameter settings may directly lead to a significant loss of α_{mean}, causing an unsuccessful acquisition, whereas proper choices can reduce the loss of α_{mean} after the ANF operation. In the simulated scenario, the best parameter settings of k_α and δ is $k_\alpha = 0.9$ and $\delta = 0.1$, and these parameters can be tuned and continuously optimized based on the value of α_{mean}. The optimized zone for the choices of k_α and δ is to fix k_α between 0.8 and 0.9, and δ between 0.05 and 0.1. In order to finalize more precise parameter settings, other variable parameters besides k_α and δ can also be tuned based on the metric. According to the investigation in [21], the threshold T_h and the forgetting factor α do not show obvious influence to maximize the value of α_{mean}, compared to the effects of k_α and δ. The proposed method for parameter optimization can also fit the FLL-equivalent ANFs [21]. Although the value of α_{mean} is significantly recovered by the optimized ANF, there is still a noticeable loss compared to the interference-free case. This is due to the vestigial signal distortion introduced by the ANF operation and the residual unmitigated interference, which cannot be avoided.

C. Bias Analysis

The bias analysis addressed in Section V for CWI and NF is hereafter extended to chirp signals and the ANF. The complexity of both the chirp and ANF models makes the estimation of the induced bias with respect to the variable characteristics more complex. A starting point is to evaluate the effects of the chirp signal on the discriminator function with different characteristics. In this regard, the S-Curve distorted by a linear chirp over 1 ms, i.e., 50 chirp periods in total with $T_p = 20\,\mu$s in this case, is illustrated in Fig. 13 as an example. The presence of a linear chirp not only leads to a bias at the zero-crossing point, but also an overall shape deformation of the S-Curve. Differently from the case of CWI, where a more regular shape deformation appears as the power of CWI increases, the shape deformation due to the linear chirp is irregular and difficult to predict.

In order to obtain the IEE for the linear chirp signal, the ranging errors over all possible chirp phases versus chirp central frequency are depicted in Fig. 14. The IEE is then achieved as a plot of the extracted maximum and minimum values of the ranging errors over all chirp phases versus chirp central frequency. The typical parameters of the chirp signal are selected to estimate the effects of the characteristics on the generation of IEE. In Fig. 15, the influence of the power of the chirp on the IEE is demonstrated by choosing three different power levels. It can be observed that the overall level of the IEE grows as the chirp

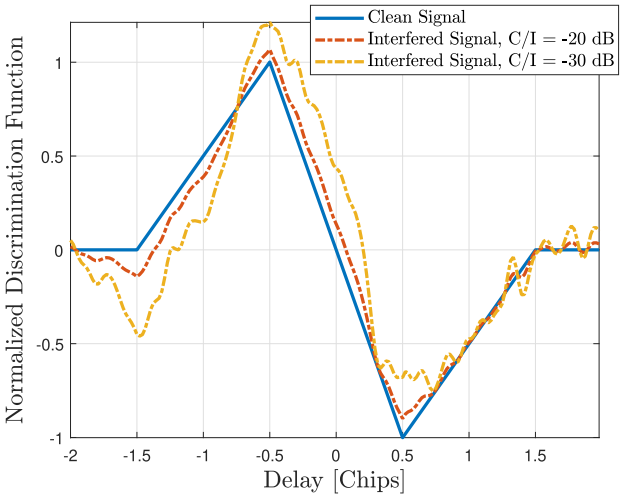

Fig. 13. S-Curve for BPSK (GPS L1, PRN 1) distorted by a linear chirp, with $B_n = 16$ MHz, $T_p = 20\,\mu$s, and $f_c = 1$ MHz.

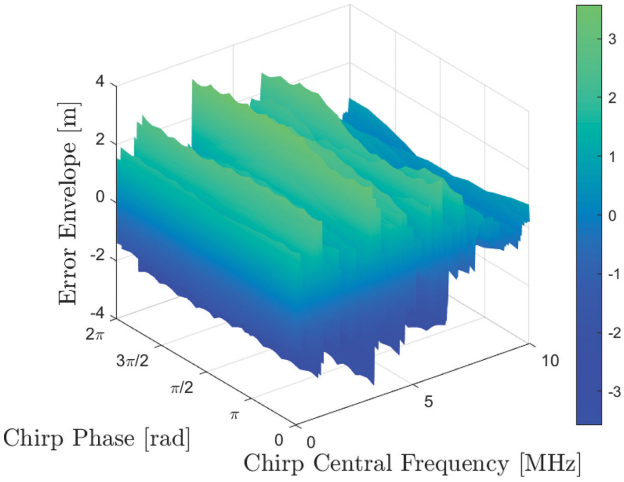

Fig. 14. Error envelope for BPSK (GPS L1, PRN 1) versus chirp phase and chirp central frequency, with $B_n = 16$ MHz, $T_p = 20\,\mu$s, and $C/I = 0$ dB.

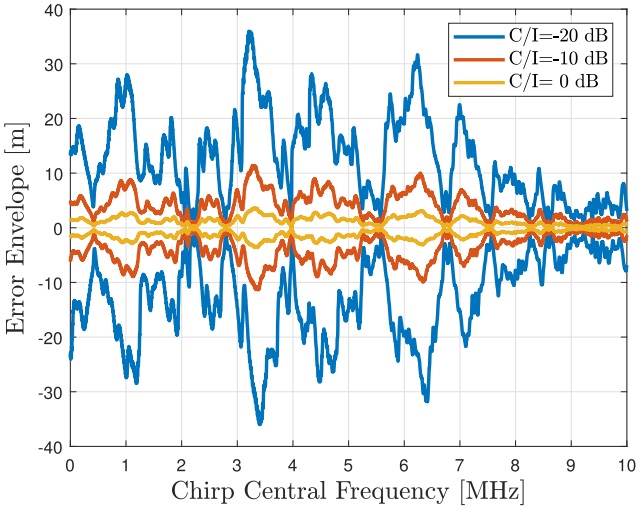

Fig. 15. IEE for the linear chirp signal for BPSK (GPS L1, PRN 1) with different C/I, with $B_n = 16$ MHz and $T_p = 20\,\mu$s.

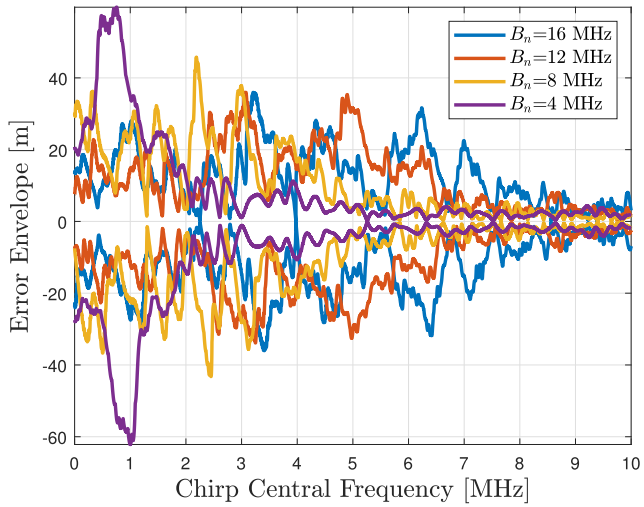

Fig. 16. IEE for the linear chirp signal for BPSK (GPS L1, PRN 1) with different B_n, with $v_s = 0.8\,\text{MHz}/\mu\text{s}$ and $C/I = -20\,\text{dB}$.

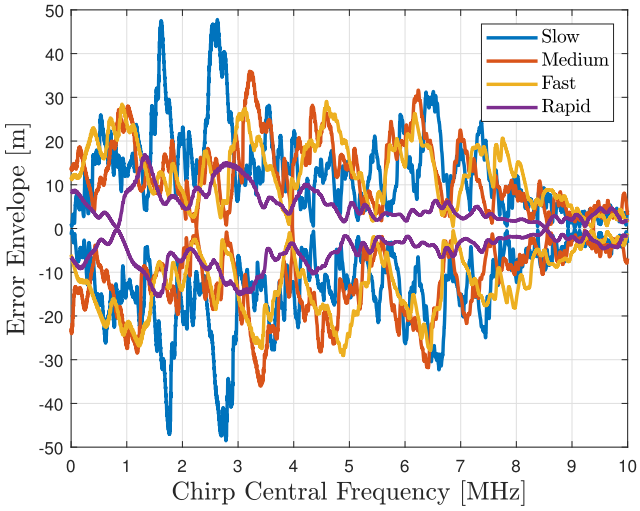

Fig. 17. IEE for the linear chirp signal for BPSK (GPS L1, PRN 1) with different v_s, with $B_n = 16\,\text{MHz}$ and $C/I = -20\,\text{dB}$.

power increases but still keeps a similar trend for different power levels. The overall shape of the IEE for the chirp signal fluctuates significantly as f_c increases when the chirp bandwidth is fully or partially covering the main lobe of the code spectrum, gradually reducing toward to zero for high f_c, where the chirp bandwidth only affects the side lobes. Although the IEE for the chirp signal is quite different from the IEE for CWI in [28] and it looks irregular, the maximum and minimum values of the ranging errors still show to be approximately symmetric. Furthermore, the overall values of the ranging errors are much smaller than the case of IEE for CWI in the case of $C/I = 0\,\text{dB}$. In Fig. 16, the sweep range of the chirp varies and the most influential effect on the envelope for each B_n appears at different f_c. For instance, a large B_n shows continuous effects on a wide range of the shift frequency, while a narrow B_n only affects a small portion, depending on the portion it covers within the main lobe of the code spectrum. However, it seems that with a medium sweep rate ($v_s = 0.8\,\text{MHz}/\mu\text{s}$), a narrow B_n produces the largest errors in terms of IEE maximum values. In addition, the sweep rate is also considered as an interesting characteristic to investigate. The sweep rate is inversely proportional to the sweep period if B_n is fixed. Four different v_s are selected on the basis of the real chirp parameters described in [5], namely slow ($v_s = 0.48\,\text{MHz}/\mu\text{s}$), medium ($v_s = 0.8\,\text{MHz}/\mu\text{s}$), fast ($v_s = 1.6\,\text{MHz}/\mu\text{s}$), and rapid ($v_s = 2.7\,\text{MHz}/\mu\text{s}$). In Fig. 17, the IEE reflects that a slower v_s brings more severe impact on the IEE, and the overall envelope decreases as the sweep rate increases.

Fig. 18 demonstrates the induced ranging errors with different discriminator spacing under the influence of a medium chirp signal. As already observed in Fig. 10, the overall ranging error reduces for smaller spacing of the discriminator, thus demonstrating more resilience to the chirp signal. The same trend can be noticed in Fig. 19, where the BOC (1, 1) modulated signal exhibits even further reduced errors if compared to the BPSK.

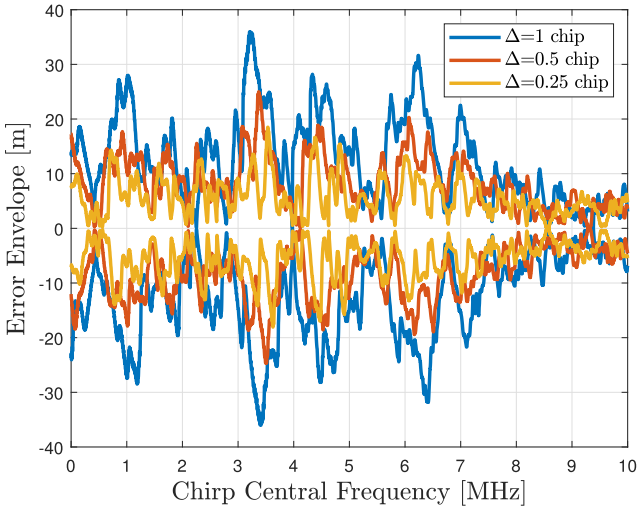

Fig. 18. IEE for the linear chirp signal for BPSK (GPS L1, PRN 1) with different spacing, with $B_n = 16\,\text{MHz}$, $T_p = 20\,\mu\text{s}$, and $C/I = -20\,\text{dB}$.

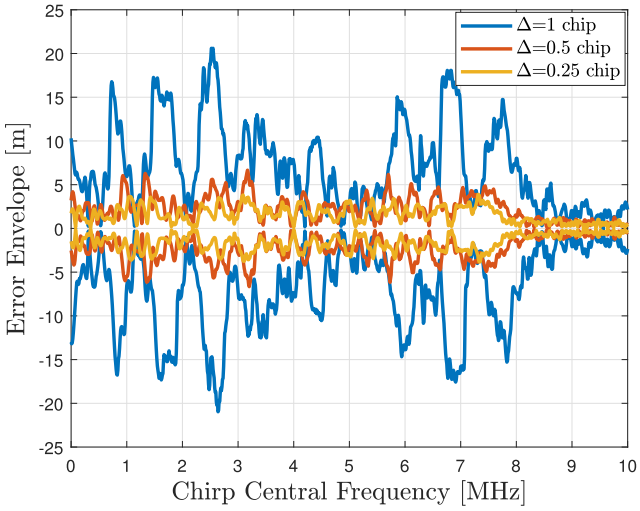

Fig. 19. IEE for the linear chirp signal for BOC (1, 1) with different spacing, with $B_n = 16\,\text{MHz}$, $T_p = 20\,\mu\text{s}$, and $C/I = -20\,\text{dB}$.

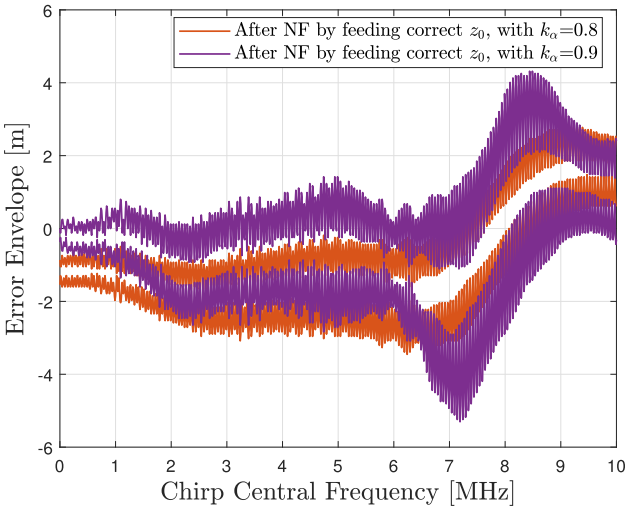

Fig. 20. IEE for the linear chirp after ideal ANF operation for BPSK (GPS L1, PRN 1).

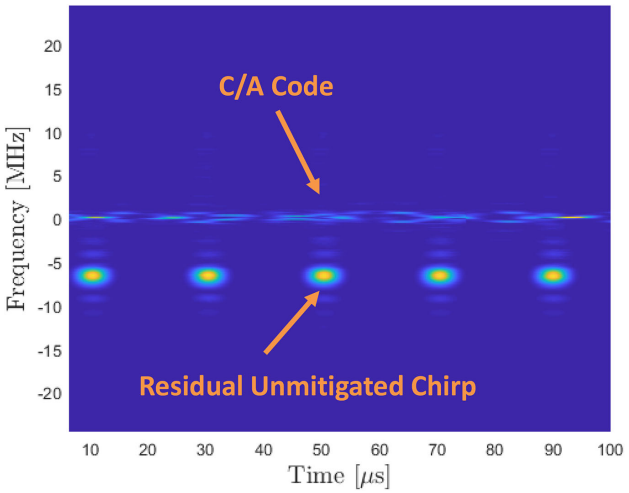

Fig. 21. Residual unmitigated chirp after ANF operation, with $B_n = 16$ MHz, $T_p = 20\,\mu$s, and $C/I = -20$ dB.

The ANF is then implemented to mitigate the chirp signal, and the effects on the IEE are investigated. In order to separately analyze the effect induced by the two main parameters, i.e., k_α and δ, the adaptive block is disabled, and the one-pole NF is fed with the true z_0 at run-time, instead of calculating z_0 according to (8). In this way, an ideal frequency tracking capability of the ANF is assumed, so that the only impact to the IEE is due to the parameter k_α. The IEE for the linear chirp after the ideal ANF is shown in Fig. 20. Two k_α are selected as exemplary values. The resulting ranging errors, after an ideal chirp mitigation, are caused by both the NF operation and the residual unmitigated chirp. It can be noted that the overall level of IEE decreases significantly and is no longer symmetric, confirming how an effective mitigation is the dominant contribution compared to the residual chirp. However, when $f_c \sim 8$ MHz, the effectiveness of the mitigation operation decreases. This can be explained by considering the transient time of the ANF in correspondence of the frequency discontinuity between two chirp repetitions. As illustrated in Fig. 21, the ANF is

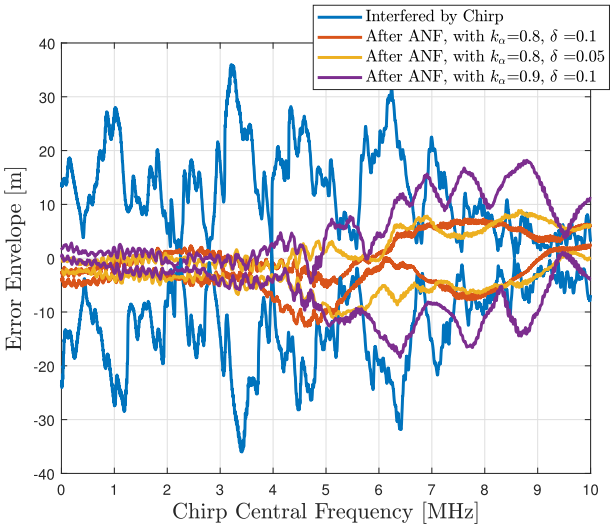

Fig. 22. IEE for the linear chirp for BPSK (GPS L1, PRN 1) after ANF operation, with $B_n = 16$ MHz, $T_p = 20\,\mu$s, and $C/I = -20$ dB.

not activated during the transient time, and a small portion of the chirp remained unfiltered at the lower part of the chirp sweep range. When $f_c \sim 8$ MHz and $B_n = 16$ MHz in the case, the remaining unfiltered chirp partially covers the main lobe of the code spectrum, leading to an increasing impact.

At last, the interfered signal is filtered by the ANF with different parameter settings of k_α and δ, with fixed $T_h = 0.7$ and $\alpha = 0.9$. In Fig. 22, the IEE after ANF mitigation with three different parameter settings is depicted. All of the three cases show effective mitigation with significant reduction of the overall envelope. The IEE trends are similar to the ones in Fig. 20, showing a clear asymmetry between maximum and minimum values and higher errors for $f_c \sim 8$ MHz. Comparing the IEE in Figs. 20 and 22, both of the two cases are with $k_\alpha = 0.8$ and $k_\alpha = 0.9$; thus, the difference is induced by the different frequency tracking capability. The former has the ideal frequency tracking capability, and the latter is limited by δ. It can be seen in Fig. 23 that after the ANF operation, both the bias at the zero-crossing point and the overall shape deformation of the S-Curve are reduced. It is worth noting that $f_c = 1$ MHz has been chosen, since at this central frequency, the error is relatively large, as shown in Fig. 22.

As already observed for the CWI, also for a chirp signal, the ANF could induce a more severe distortion than the interference itself in the case of inappropriate parameter settings. In addition, as the receiver configuration (e.g., Δ), the characteristics of the chirp signal (e.g., P_{cp}, B_n, T_p, and f_c) and the ANF parameters (e.g., k_α and δ) change, the distortion on the S-Curve and the error envelope could be very different.

D. Jitter Analysis

The jitter analysis is based on the same simulation setup used for the α_{mean} analysis at the acquisition stage as reported in Section VI-B. As reference, the code jitter in scenarios with and without interference is, respectively,

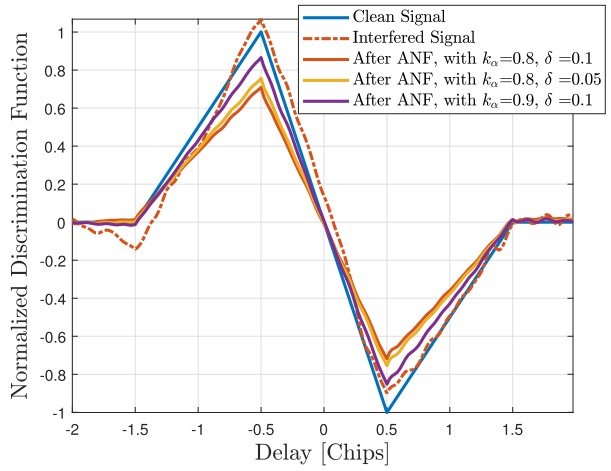

Fig. 23. S-Curve distortion after ANF operation for BPSK (GPS L1, PRN 1), with $B_n = 16$ MHz, $T_p = 20\,\mu$s, $f_c = 1$ MHz, and $C/I = -20$ dB.

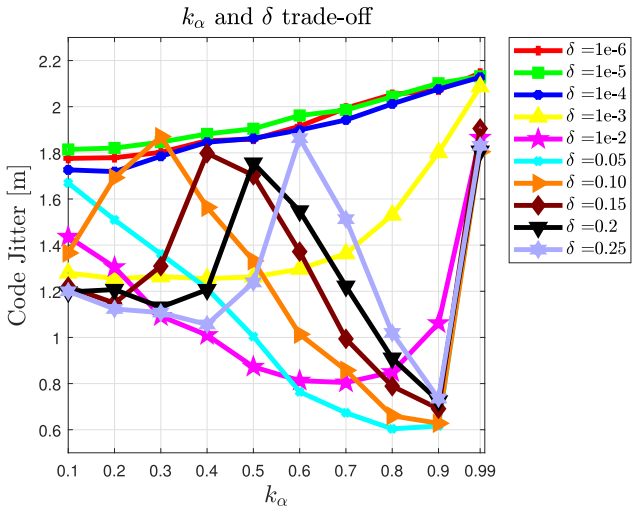

Fig. 24. k_α and δ tradeoff based on code jitter, with $B_n = 16$ MHz, $T_p = 20\,\mu$s, and $C/I = -50$ dB.

calculated as 2.13 and 0.42 m. The difference between these two values can quantitatively reflect the impairment due to the chirp signal at the tracking stage.

In Fig. 24, the plot of code jitter expressed in meters as a function of k_α and δ is depicted. It can be observed that the value of code jitter differs significantly as the parameters change. A smaller value of the code jitter indicates a more effective chirp mitigation, with less induced bias and overall deformation of the S-Curve. Thus, the optimized configuration for the ANF can be obtained with k_α fixed between 0.8 and 0.9 and δ between 0.05 and 0.1 (see the light blue and orange plots). In particular, the combination $k_\alpha = 0.8$ and $\delta = 0.05$ results in a code jitter close to 0.60 m, showing the optimal performance achievable after the ANF operation. Based on the value of code jitter, it can be seen that even after the optimized filtering operation, the residual error is not negligible if compared to the interference-free case.

Similar to the use of α_{mean}, the metric of code jitter can also indicate the ANF efficiency at the tracking stage, thus optimizing the parameter configurations. Furthermore, comparing Figs. 12 and 24, the two metrics at two signal processing stages lead to similar optimized configurations for the ANF. It seems to indicate that a good tradeoff between k_α and δ can maximize both the acquisition and tracking performance along the signal processing chain based on the proposed metrics. This can help to find the optimal configuration for the ANF.

VII. CONCLUSION

This article has addressed the problem of the impact of the ANF operation for chirp removal in the signal processing stages of GNSS receivers. As already extensively discussed, the performance of the ANF is strongly dependent on its configuration setup. Inappropriate parameter settings of the ANF can bring severe distortion to the correlation process, leading to an outage of the receiver service. Three metrics have been proposed as assessment tools to quantitatively evaluate the effects.

The investigation first goes to the bias analysis in the case of NF for CWI cancellation. The NEE is proposed as the metric to quantitatively estimate the impairment merely by the NF operation at the tracking stage. Similar to the IEE, the NEE is a plot of ranging errors versus the parameters that regulate the NF performance, namely the rejection bandwidth and the frequency of the notch. Although both the interference and the NF operation can separately affect the S-Curve with an induced bias at the zero-crossing point, the mechanism behind it is different. This is reflected in the different shapes of the IEE and the NEE, as illustrated in Section V. Good mitigation of CWI by means of an NF does not guarantee zero code biases. On the contrary, a residual bias resulting from the combination of the filtering operation and the unfiltered residual interference can be observed, up to tens of meters depending on interference frequency and other parameters. When CWI is efficiently cancelled, then the distortion and biases caused by notch filtering are dominant with respect to the residual unmitigated interference. Additionally, a further bias compensation process is proposed that can be performed by excluding the NEE for each PRN. The IEE after compensation process is isolated from the deterministic notch filtering effects.

A more complex scenario is the comparative analysis of the impact of the ANF for chirp removal. The proposed three metrics are employed to assess the effects at both the acquisition stage and the tracking stage. The use of α_{mean} can depict a direct picture of the optimal performance achievable with different configurations of the ANF at the acquisition stage; thus, the optimized zone for parameter settings can be obtained. An inappropriate configuration setup may cause severe effects to the correlation process and lead to significant loss of α_{mean}. Therefore, it provides an instrument to estimate the impairment due to the ANF operation by considering the loss of α_{mean} compared to the interference-free case.

The investigation is further carried out at the tracking stage by using the metrics of IEE and code jitter. The roles of

the two metrics are different. The use of IEE aims to estimate the maximum distortions versus the variable characteristics to have a more comprehensive understanding on the most influential parameters of the chirp (e.g., P_{cp}, B_n, T_p, and f_c) and the ANF (e.g., k_α and δ) at the tracking stage. However, because of the fact that the S-Curve may be irregularly distorted by the chirp signal, the overall shape deformation of the S-Curve is also taken into account by estimating the code jitter. Based on the IEE, the plot of ranging errors versus the variable parameters of the chirp and the ANF is depicted. Similar to the use of α_{mean}, the optimal achievable performance on the basis of code jitter can be directly obtained. The impairment due to the ANF operation can be assessed by comparing the value of code jitter to the interference-free case. In addition, it seems indicating that one good configuration setup for the ANF can maximize both the acquisition and tracking performance in GNSS receivers. This needs to be verified on other types of chirp signals and receiver configurations. For instance, a performance comparison of different discriminator architectures, both coherent and noncoherent, could be performed in the next future, in order to find the best tracking algorithms to be used when the ANF is performed.

REFERENCES

[1] F. Dovis
Ed., *GNSS Interference Threats and Countermeasures*. Norwood, MA, USA: Artech House, 2015.

[2] B. Motella, M. Pini, and F. Dovis
Investigation on the effect of strong out-of-band signals on global navigation satellite systems receivers
GPS Solutions, vol. 12, no. 2, pp. 77–86, Mar. 2008.

[3] W. Qin and F. Dovis
Effects of interference mitigation methods on scintillation detection
In *Proc. 9th ESA Workshop Satell. Navigat. Technol./Eur. Workshop GNSS Signals Signal Process.*, Dec. 2018, pp. 1–8.

[4] R. H. Mitch *et al.*
Signal characteristics of civil GPS jammers
In *Proc. 24th Int. Techn. Meeting Satell. Division Instit. Navigat.*, Portland, OR, USA, Sep. 2011, pp. 1907–1919.

[5] M. Pattinson, S. Lee, Z. Bhuiyan, S. Thombre, V. Manikundalam, and S. Hill
D4.2: Draft standards for receiver testing against threats
STRIKE3 Public Deliverable, Nov. 2017.

[6] L. Musumeci and F. Dovis
Effect of pulse blanking on navigation data demodulation performance in GNSS system
In *Proc. IEEE/ION Position, Location Navigat. Symp.*, May 2014, pp. 1248–1257.

[7] L. Musumeci, J. Samson, and F. Dovis
Performance assessment of pulse blanking mitigation in presence of multiple distance measuring equipment/tactical air navigation interference on global navigation satellite systems signals
IET Radar, Sonar Navigat., vol. 8, no. 6, pp. 647–657, Jul. 2014.

[8] M. Raimondi, O. Julien, C. Macabiau, and F. Bastide
Mitigating pulsed interference using frequency domain adaptive filtering
In *Proc. 19th Int. Tech. Meeting Satell. Division Inst. Navigat.*, Fort Worth, TX, USA, Sep. 2006, pp. 2251–2260.

[9] S. Savasta, L. Lo Presti, and M. Rao
Interference mitigation in GNSS receivers by a time-frequency approach
IEEE Trans. Aerosp. Electron. Syst., vol. 49, no. 1, pp. 415–438, Jan. 2013.

[10] L. Musumeci and F. Dovis
Use of the wavelet transform for interference detection and mitigation in global navigation satellite systems
Int. J. Navigat. Observ., vol. 2014, pp. 1–14, Mar. 2014.

[11] F. Dovis and L. Musumeci
Use of the Karhunen-Loève transform for interference detection and mitigation in GNSS
ICT Express, vol. 2, no. 1, pp. 33–36, 2016.

[12] R. Rifkin and J. J. Vaccaro
Comparison of narrowband adaptive filter technologies for GPS
In *Proc. IEEE Position Location Navigat. Symp.*, Mar. 2000, pp. 125–131.

[13] D. Borio, L. Camoriano, and P. Mulassano
Analysis of the one-pole notch filter for interference mitigation: Wiener solution and loss estimations
In *Proc. 19th Int. Tech. Meeting Satell. Division Inst. Navigat.*, Fort Worth, TX, USA, Sep. 2001, pp. 1849–1860.

[14] D. Borio, L. Camoriano, and L. L. Presti
Two-pole and multi-pole notch filters: A computationally effective solution for GNSS interference detection and mitigation
IEEE Syst. J., vol. 2, no. 1, pp. 38–47, Mar. 2008.

[15] J. W. Choi and N. I. Cho
Suppression of narrow-band interference in DS-spread spectrum systems using adaptive IIR notch filter
Signal Process., vol. 82, no. 12, pp. 2003–2013, 2002.

[16] T. T. N. Tu, V. L. The, T. H. Ta, H. L. T. Nguyen, and B. Motella
An adaptive bandwidth notch filter for GNSS narrowband interference mitigation
J. Electron. Commun., vol. 4, nos. 3/4, pp. 59–68, Jul. 2014.

[17] G. X. Gao
DME/TACAN interference and its mitigation in L5/E5 bands
In *Proc. 20th Int. Tech. Meeting Satell. Division Inst. Navigat.*, Fort Worth, TX, USA, Sep. 2007, pp. 1191–1200.

[18] D. Borio
Loop analysis of adaptive notch filters
IET Signal Process., vol. 10, no. 6, pp. 659–669, 2016.

[19] M. T. Gamba and E. Falletti
Performance analysis of FLL schemes to track swept jammers in an adaptive notch filter
In *Proc. 9th ESA Workshop Satell. Navigat. Technol./Eur. Workshop GNSS Signals Signal Process.*, Dec. 2018, pp. 1–8.

[20] M. T. Gamba and E. Falletti
Performance comparison of FLL adaptive notch filters to counter GNSS jamming
In *Proc. Int. Conf. Localization GNSS*, Jun. 2019, pp. 1–6.

[21] W. Qin, F. Dovis, M. T. Gamba, and E. Falletti
A comparison of optimized mitigation techniques for swept-frequency jammers
In *Proc. Int. Tech. Meeting Inst. Navigat.*, Reston, VA, USA, Jan. 2019, pp. 233–247.

[22] G. Giordanengo
Impact of notch filtering on tracking loops for GNSS applications
master's thesis, Facoltà di Ingegneria dell'informazione, Politecnico di Torino, Turin, Italy, 2009.

[23] M. T. Gamba, E. Falletti, D. Rovelli, and A. Tuozzi
FPGA implementation issues of a two-pole adaptive notch filter for GPS/Galileo receivers
In *Proc. 25th Int. Tech. Meeting Satell. Division Inst. Navigat.*, 2012, pp. 3549–3557.

[24] J. Raasakka and M. Orejas
Analysis of notch filtering methods for narrowband interference mitigation
In *Proc. IEEE/ION Position, Location Navigat. Symp.*, Monterey, CA, USA, May 2014, pp. 1282–1292.

[25] W. Qin, F. Dovis, M. T. Gamba, and E. Falletti
Effects of optimized mitigation techniques for swept-frequency jammers on tracking loops
In *Proc. 32nd Int. Tech. Meeting Satell. Division Inst. Navigat.*, Miami, FL, USA, Sep. 2019, pp. 3275–3284.

[26] V. Calmettes, F. Pradeilles, and M. Bousquet
Study and comparison of interference mitigation techniques for GPS receiver
In *Proc. 14th Int. Tech. Meeting Satell. Division Inst. Navigat.*, Salt Lake City, UT, USA, Sep. 2001, pp. 957–968.

[27] B. Motella, S. Savasta, D. Margaria, and F. Dovis
A method to assess robustness of GPS C/A code in presence of CW interferences
Int. J. Navigat. Observ., vol. 2010, pp. 1–8, 2010.

[28] B. Motella, S. Savasta, D. Margaria, and F. Dovis
Method for assessing the interference impact on GNSS receivers
IEEE Trans. Aerosp. Electron. Syst., vol. 47, no. 2, pp. 1416–1432, Apr. 2011.

[29] E. Kaplan and C. Hegarty
Understanding GPS: Principles and Applications. Norwood, MA, USA: Artech House, 2005.

[30] D. Borio, C. Mongredien, and G. Lachapelle
Collaborative code tracking of composite GNSS signals
IEEE J. Sel. Topics Signal Process., vol. 3, no. 4, pp. 613–626, Aug. 2009.

[31] E. Falletti, D. Margaria, M. Nicola, G. Povero, and M. T. Gamba
N-FUELS and SOPRANO: Educational tools for simulation, analysis and processing of satellite navigation signals
In *Proc. IEEE Frontiers Educ. Conf.*, Oklahoma City, OK, USA, 2013, pp. 303–308.

[32] L. L. Presti, P. di Torino, E. Falletti, M. Nicola, and M. T. Gamba
Software Defined Radio technology for GNSS receivers
In *Proc. IEEE Metrol. Aerosp.*, May 2014, pp. 314–319.

[33] J. O. Smith
Introduction to Digital Filters: With Audio Applications, vol. 2. W3K Publishing, 2007. [online]. Available: http://books.w3k.org/

Wenjian Qin received the B.Eng. degree from Wuhan University, Wuhan, China, in 2010 and the M.Sc. degree from the University of Stuttgart, Stuttgart, Germany, in 2012 both in geomatics engineering. He is currently working toward the Ph.D. degree with the Navigation Signal Analysis and Simulation Group, Department of Electronics and Telecommunications, Politecnico di Torino, Torino, Italy.

He is also a Marie Skłodowska–Curie Research Fellow within the TREASURE Project funded by the European Union's Horizon 2020 Research and Innovation Programme. His research interests include the global navigation satellite system interference detection and mitigation techniques.

Micaela Troglia Gamba received the M.Sc. and Ph.D. degrees in electronics engineering from the Politecnico di Torino, Torino, Italy, in 2007 and 2011, respectively.

She is currently a Researcher with the Space and Navigation Technologies Area, LINKS Foundation, Torino, working as a hardware–software designer and developer of new digital architectures for global navigation satellite system (GNSS) receivers. Her main research include the implementation of interference detection and mitigation algorithms on real-time GNSS software receivers, running on general-purpose processors, and low-cost ARM-based embedded platforms.

Emanuela Falletti received the M.Sc. and Ph.D. degrees in electronics and communications engineering from Politecnico di Torino, Italy, in 1999 and 2004, respectively.

She is the Leader of the Systems Analysis and Simulation Research Team, Space and Navigation Technologies Area, LINKS Foundation, Torino, Italy. She has authored several scientific papers for journals and international conferences and acts as a peer reviewer for various scientific publications. Her research interests include digital signal processing and simulation techniques for global navigation satellite system software receivers, including signal quality monitoring, interference, and spoofing monitoring, and multiantenna processing.

Fabio Dovis received the M.Sc. and Ph.D. degrees in electronics and communications engineering both from the Politecnico di Torino, Torino, Italy, in 1996 and 2000, respectively.

He is an Associate Professor with the Department of Electronics and Telecommunications, Politecnico di Torino, Torino, Italy, where he coordinates the Navigation Signal Analysis and Simulation Group. His research interests include the design of GPS and Galileo receivers and advanced signal processing for interference and multipath detection and mitigation, as well as ionospheric monitoring.

Prof. Dovis is a member of the Navigation Systems Panel of the IEEE Aerospace and Electronic Systems Society. He has a relevant experience in international projects in cooperation with industries in the field of satellite navigation.